RESEARCH ARTICLE

Image Derived Input Function for [^{18}F]-FEPPA: Application to Quantify Translocator Protein (18 kDa) in the Human Brain

Rostom Mabrouk[1]*, Pablo M. Rusjan[1], Romina Mizrahi[1,5], Mark F. Jacobs[3], Yuko Koshimori[1,3], Sylvain Houle[1], Ji Hyun Ko[4], Antonio P. Strafella[1,2,3]

1. Research Imaging Centre, Centre for Addiction and Mental Health (CAMH), Toronto, Ontario, Canada, **2.** Morton and Gloria Shulman Movement Disorder Unit, E.J. Safra Parkinson Disease Program, Toronto Western Hospital, UHN, University of Toronto, Toronto, Canada, **3.** Division of Brain, Imaging and Behaviour, Systems Neuroscience, Toronto Western Research Institute, UHN, University of Toronto, Toronto, Ontario, Canada, **4.** Department of Human Anatomy and Cell Science, University of Manitoba, Winnipeg, Manitoba, Canada, **5.** Department of Psychiatry, University of Toronto, Toronto, Ontario, Canada

*rostom.mabrouk@camh.ca

Data Availability: The authors confirm that, for approved reasons, some access restrictions apply to the data underlying the findings. All relevant data are within the paper and its Supporting Information files.

Competing Interests: The authors have declared that no competing interests exist.

Abstract

In [^{18}F]-FEPPA positron emission topography (PET) imaging, automatic blood sampling system (ABSS) is currently the gold standard to obtain the blood time activity curve (TAC) required to extract the input function (IF). Here, we compare the performance of two image-based methods of IF extraction to the ABSS gold standard method for the quantification of translocator protein (TSPO) in the human brain. The IFs were obtained from a direct delineation of the internal carotid signal (CS) and a new concept of independent component analysis (ICA). PET scans were obtained from 18 healthy volunteers. The estimated total distribution volume (V_T) by CS-IF and ICA-IF were compared to the reference V_T obtained by ABSS-IF in the frontal and temporal cortex, cerebellum, striatum and thalamus regions. The V_T values estimated using ICA-IF were more reliable than CS-IF for all brain regions. Specifically, the slope regression in the frontal cortex with ICA-IF was $r^2=0.91$ ($p<0.05$), and $r^2=0.71$ ($p<0.05$) using CS-IF.

Introduction

Neuroinflammation has been implicated to play a role in the pathogenesis of various conditions including Alzheimer's disease [1], stroke [2], Parkinson's disease [3, 4] and epilepsy [5]. In general, neuroinflammation is characterized by

an overexpression of the translocator protein 18 kDa (TSPO) in activated microglia [6]. Using radioligands that bind to TSPO, positron emission tomography (PET) is able to measure neuroinflammation in the human brain *in vivo* by quantifying TSPO density. The most commonly used radioligand over the last decade has been [11C] (R)-PK 11195 [7]. However, [11C] (R)-PK 11195 has several disadvantages including low penetration into brain tissue and poor specificity [8]. These limitations triggered interest for the development of new radioligands to overcome the issues above, such as [18F]-FEPPA [9], [11C]-PBR28 [10], [18F]-PBR06 [11], [18F]-PBR111 [12], [11C]-DAA1106 [13], [11C]-DPA-713 [14], and [11C]-AC-5216 [15]. Of particular interest, [18F]-FEPPA rapidly penetrates brain tissue and has a high affinity and selectivity to TSPO [16] and is, therefore, a favorable radiotracer to quantify TSPO in the human brain.

The quantification of TSPO in dynamic PET data requires an input function (IF) that estimates the arterial plasma radioactivity. For [18F]-FEPPA PET imaging, an automatic blood sampling system (ABSS) is currently the gold standard to obtain the blood time activity curve (TAC) required to extract the IF. The blood sampling for [18F]-FEPPA PET analysis is often taken at a continuous rate of 2.5 mL/min for the first 22.5 minutes. The main advantage of ABSS is the accurate peak-detection of the IF, which is subsequently used in the kinetic modeling. However, the large volume of blood sampled and the arterial catheterization could induce a physiological effect, infection and/or occlusion [17]. Moreover, ABSS is a costly and time-consuming protocol. Over the years, many researchers have proposed alternative methods to derive the IF in order to minimize the need for repeated blood sampling. One technique extracts the IF directly from PET image data in order to estimate the whole-blood and plasma TACs. Using this method, investigators have successfully obtained the IF from image sources such as the left ventricle to estimate myocardial metabolic rate of glucose (MRGlu) [18, 19] and femoral arteries data from PET imaging to estimate perfusion index in the femoral muscle [20]. In the human brain, the internal carotid artery signal (CS) has been used to extract blood TAC [21, 22]. However, the poor spatial resolution of PET relative to the size of the artery and motion effect which is mostly not easily addressed causes estimation errors [23]. Alternatively, the IF can be obtained from a blind-source separation technique, such as independent component analysis (ICA) [24]. This objective method identifies cranial blood pools and extracts the blood activity signal without the need for manual segmentation of arteries. Further, ICA decreases the noise effect in the blood activity by keeping the principal component and minimizes the noise component corresponding to the lowest eigenvalues (for review, see [24]). Importantly, the success of the ICA approach largely depends on tracer characteristics such as kinetics, washout, tissue distribution, and metabolite formation. Thus, each radiotracer may require an optimized method for ICA. For example, the EPICA algorithm has been demonstrated to accurately describe the FDG tracer in PET imaging [24]. Given the unique tracer kinetics of [18F]-FEPPA, the tracer is very likely to require an optimized ICA algorithm.

Although a few studies with [11C]-(R)-PK11195 has employed reference tissue model thanks to its low affinity [25, 26] no suitable reference region with negligible binding has been identified for the high affinity 2nd generation TSPO radiotracers such as [^{18}F]-FEPPA. Therefore arterial IF must be obtained to quantify receptor binding. Two common analytic approaches are the graphical plot [27] and compartment model. Our group has previously shown that the two-tissue compartment model (2-TCM) accurately describes the [^{18}F]-FEPPA tissue TACs and produces a total distribution volume (V_T) estimation [16]. In this previous work, ABSS together with manual arterial blood samples were used to generate the IF. In the current study, we aim to find an alternative to ABSS in [^{18}F]-FEPPA PET imaging for reasons stated above, namely practicality. For this purpose, we compare the performance of the ABSS with two methods of IF extraction; a) direct delineation of the CS and b) a modified ICA algorithm. We introduce a new concept for the ICA algorithm based on an Asymmetric Laplace distribution (ALD) [28] to improve compatibility with blood region activity features. To test for the interchangeability of the two methods with the ABSS gold standard, we first compared the shape and the area under curve (AUC) of the IFs generated by each method. Subsequently, the linear regression analysis and the Bland-Altman plot were used to test the interchangeability and reliability of the V_T estimation given by each method. To further support our modified ICA method for [^{18}F]-FEPPA modelling, the proposed ALDICA algorithm is compared to two other known, published ICA methods; EPICA and GGD-ICA. In order to demonstrate the practical applications of the proposed approaches, the estimated V_T of each method was compared group-wise between subjects categorized as mixed affinity binders (MABs) and high affinity binders (HABs) [29, 30].

Materials and Methods

1 Human subjects

Eighteen healthy volunteers (7 males, 11 females; aged 24 to 73 years) completed this study. Participants were classified into two groups according to their TSPO polymorphism genotyping (see section below). Nine subjects were classified as MABs and nine subjects as HABs. All procedures were fully explained and subjects provided written informed consent and were approved by the Centre for Addiction and Mental Health Ethics Review Board and conformed to the *Declaration of Helsinke.*

2 Polymorphism genotyping

Genomic DNA was obtained from peripheral leukocytes using high salt extraction methods [31]. The polymorphism rs6971 was genotyped variously using a TaqMan assay on demand C_2512465_20 (AppliedBiosystems, CA, USA). The allele T147 was linked to Vic and the allele A147 was linked FAM. PCR reactions

were performed in a 96-well microtiter-plate on a GeneAmp PCR System 9700 (Applied Biosystems, CA, USA). After PCR amplification, endpoint plate read and allele calling was performed using an ABI 7900 HT (Applied Biosystems, CA, USA) and the corresponding SDS software (v2.2.2). Individuals with genotype Ala147/Ala147 were classified as high affinity binders (HAB), Ala147/Thr147 as mixed affinity binders (MAB), and Thr147/Thr147 as low affinity binders (LAB) [32].

3 Positron emission tomography

All experiments were performed on a 3D high-resolution research tomograph (HRRT) PET scanner (CPS/Siemens, Knoxville, TN, USA). The scanner is made of eight planar detector heads containing LSO/LYSO phoswich detectors, with each crystal element measuring $2.2 \times 2.2 \times 10$ mm^3 and produces 207 image planes. The field of view (FOV) measures 25 cm in axial direction and 35 cm in transaxial direction. The HRRT is characterized by an isotropic spatial resolution of ~2.5 mm in all 3 directions at the center of the FOV [33]. Each subject was scanned for 120 minutes of dynamic acquisitions in list-mode on the HRRT scanner and images were reconstructed into $256 \times 256 \times 207$ cubic voxels measuring $1.22 \times 1.22 \times 1.22$ mm^3 as scheduled below using two algorithms: filtered back projection (FBP) [34] and ordered subset expectation maximization with point spread function (OSEM+PSF) reconstruction [35]. The first frames were of variable length depended on the time between the start of acquisition and the signal recorded in the FOV in both reconstruction algorithms. The subsequent FBP reconstructed image frames were defined as 5×30, 1×45, 2×60, 1×90, 1×120, 1×210, and 22×300 seconds. The subsequent OSEM reconstructed image frames were defined as 2×7, 2×8, 3×10, 2×15, 2×30, 1×45, 2×60, 1×90, 1×120, 1×210, and 22×300 seconds.

4 Magnetic resonance imaging

Magnetic resonance imaging (MRI) scans were acquired for subjects using a General Electric (Milwaukee, WI, USA) Sigma 1.5 T MRI scanner. The slice thickness measured 2 mm and the repetition time was greater than 5.300 milliseconds. The echo time=13 milliseconds and the flip angle=90°. The acquisition matrix measures 256×256, and the FOV measures 22 cm. 2D axial proton density (PD) MRI images were utilized for anatomic delineation of the cerebellum, the frontal and temporal cortex, striatum, and thalamus regions using in-house software, ROMI [36]. A discrete cosine transform (DCT) was used to wrap the standard template of ROIs to each subject.

5 Blood sampling

Approximately 185 ± 20 MBq (5 ± 0.5 mCi) of [^{18}F]-FEPPA was administered intravenously as a bolus injection. During PET acquisition, the whole-blood radioactivity was continuously measured via a cannulation to the radial artery and

using ABSS (Model #PBS-101 from Veenstra Instruments, Joure, Netherlands) at a rate of 2.5 ml/min for the first 22.5 min. Manual arterial blood samples of 4–10 ml were taken at 1.5, 2.5, 7, 15, 30, 45, 60, and 90 minutes in order to assess the concentration ratio of radioactivity in whole blood to the plasma and to calculate the metabolite composition in the plasma. The blood-to-plasma ratio was fitted by a bi-exponential. Plasma composition was determined using Hilton method [37] and the fraction of the un-metabolized radioligand was fitted by a Hill function $H(t) = \frac{\alpha \times t^\beta}{t^\beta + \gamma}$ in order to correct plasma TACs for metabolite. The correction for delay and dispersion of the radioligand was performed as follows: the delay between the manual plasma activity and the activity recorded over 50 seconds in the FOV was fitted to an irreversible 1-compartment model with whole-blood activity as an input function. The dispersion effect in the ABSS line was modeled as $C_{ABSS}(t) = \frac{1}{\tau} . e^{-\frac{t}{\tau}} \otimes C_w(t)$ [38], where C_w is the concentration of tracer in the whole-blood at time t and τ as taken equal to 16 seconds. The ABSS whole-blood radioactivity corrected for the dispersion and delay effects was used to build the input function as follows:

$$IF = \frac{C_w \times \text{metabolite correction}}{\text{Blood-to-plasma ratio}} \qquad (1)$$

The tissue TACs were generated using in-house software ROMI. A standard template of ROIs was fitted to each subject's MRI. The MRI was co-registered (SPM2, Department of Cognitive Neurology, London) to a time-average of the dynamic PET images and the transformation was subsequently applied to the ROI map. TACs were extracted from each ROI placed in the dynamic PET images.

6 Internal carotid signal delineation

The carotid ROIs were automatically delineated over the PET images. The binary masks were created by thresholding the mean image of the first 10 frames (2 minutes of scan) at $0.48 \times$ maximum intensity in which the optimal shape of the carotid artery was clearly displayed in the image series (N.B. The threshold has been determined empirically). For [18F]-FEPPA, the whole-blood TAC was extracted from the carotid ROIs as a mean of the ten highest pixel activities per plane, as explained elsewhere [22]. Only those voxels located within the lowest 36 planes (43.9 mm) were considered as carotid signal (Fig. 1).

7 Independent component analysis

The same intensity threshold ($0.48 \times$ maximum) was used to segment blood region ROIs of the brain as described in the CS methodology. The blood ROIs were applied to include the whole vascular system in brain constitute of arterial and venous activity for the ICA algorithm in order to enhance the presence of two
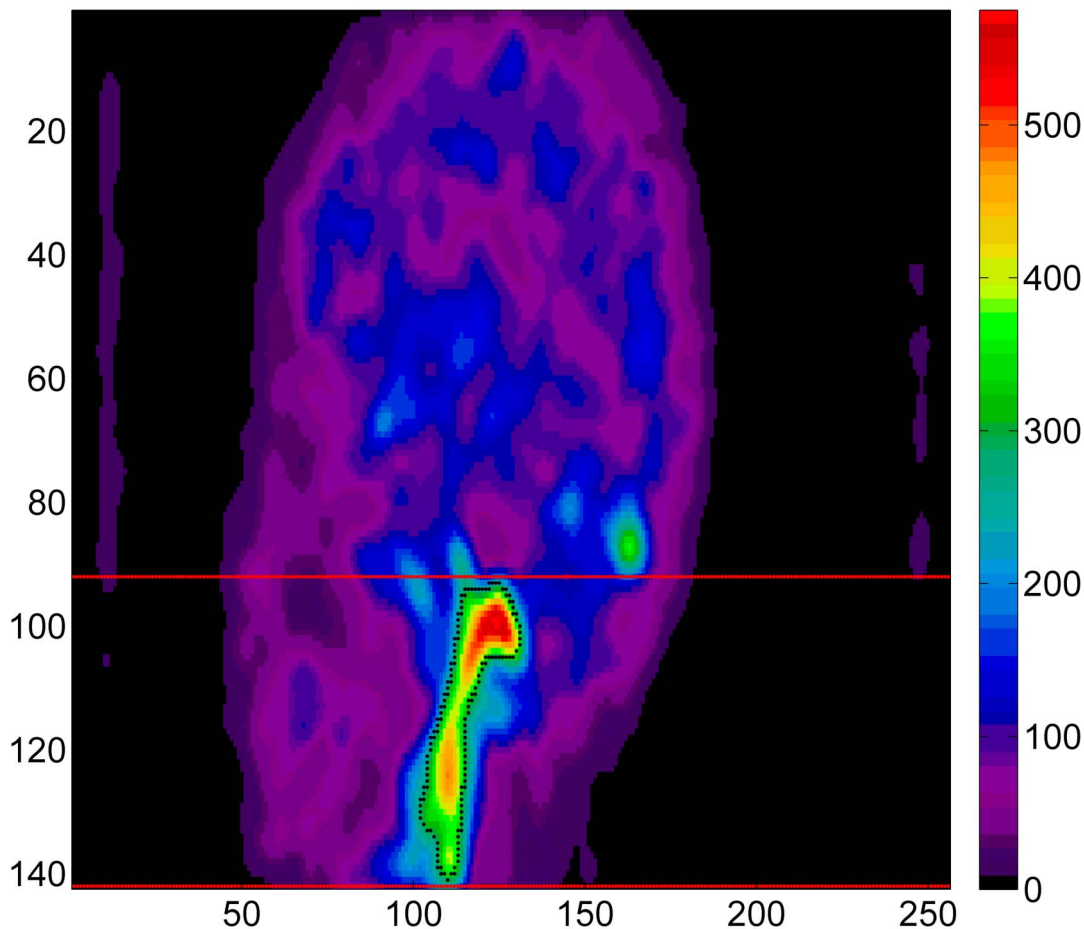
Fig. 1. Internal carotid segmentation performed on OSEM-PSF images using automatic thresholding for one subject. The red lines illustrate the lowest 36 planes containing the internal carotid artery. The black line surrounding the carotid artery represents the automatic binary mask.

different spatial distributions. Additionally, a 3D cubic Gaussian filter with FWHM=3 mm was used to smooth activity within the blood ROIs (Fig. 2).

Masks were applied to the rest of the dynamic image series to select the time activity of voxels within the blood ROIs. The 4D data were rearranged into a 2D matrix (M_{2D}). The first dimension (T) is the time course and the second dimension (Npx) is the spatial distribution of pixels in each ROI. Specifically, arterial and venous activity was largely identified in addition to the undesired signal. The dimension of M_{2D} was reduced from $T \times Npx$ to $n \times Npx$ (where n is the number of independent components of interest *e.g.* arterial and venous activity) using the principal component analysis algorithm. This technique determines the Eigenvectors (E_{eve}) and Eigenvalues (E_{eva}) of the covariance matrix $E\{M_{2D}M_{2D}{}^T\}$ and uses them as a basis for the reduction. A flow diagram of the overall process is illustrated (Fig. 3). Specifically, the matrix of the mixture of the n independent sources X was computed as a product $E_{eve}.M_{2D}$ and used as the input data in the ICA algorithm [39].
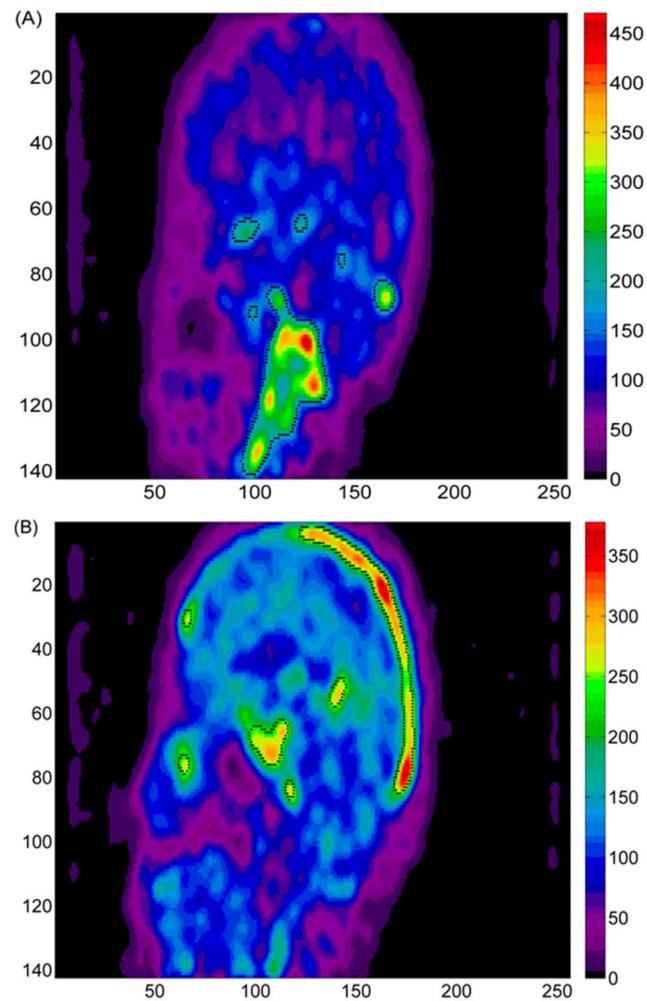
Fig. 2. ROIs extracted for the ICA algorithm for the same subject in Fig. 1. Binary masks were created from the time-averaged image (first 10 frames) and applied onto each plane to automatically select the whole-brain blood regions over all planes. A) depict the arterial activity. B) depict the superior sagittal sinus.

The matrix X is then defined as:

$$X = AS, \tag{2}$$

where the matrices S and A are unknown and X is the mixed activity. The ICA algorithm allows for estimation of S through a de-mixing matrix $\mathbf{W} = \mathbf{A}^{-1}$. Hence, the source matrix S is approximated by an estimate $\tilde{S}$ given by:

$$\tilde{S} = WX. \tag{3}$$

In this work, we used the maximum likelihood estimation to determine $\mathbf{W}$. For this purpose, we defined the negative of the log likelihood as a cost function, as defined by the Amiri algorithm [40]:
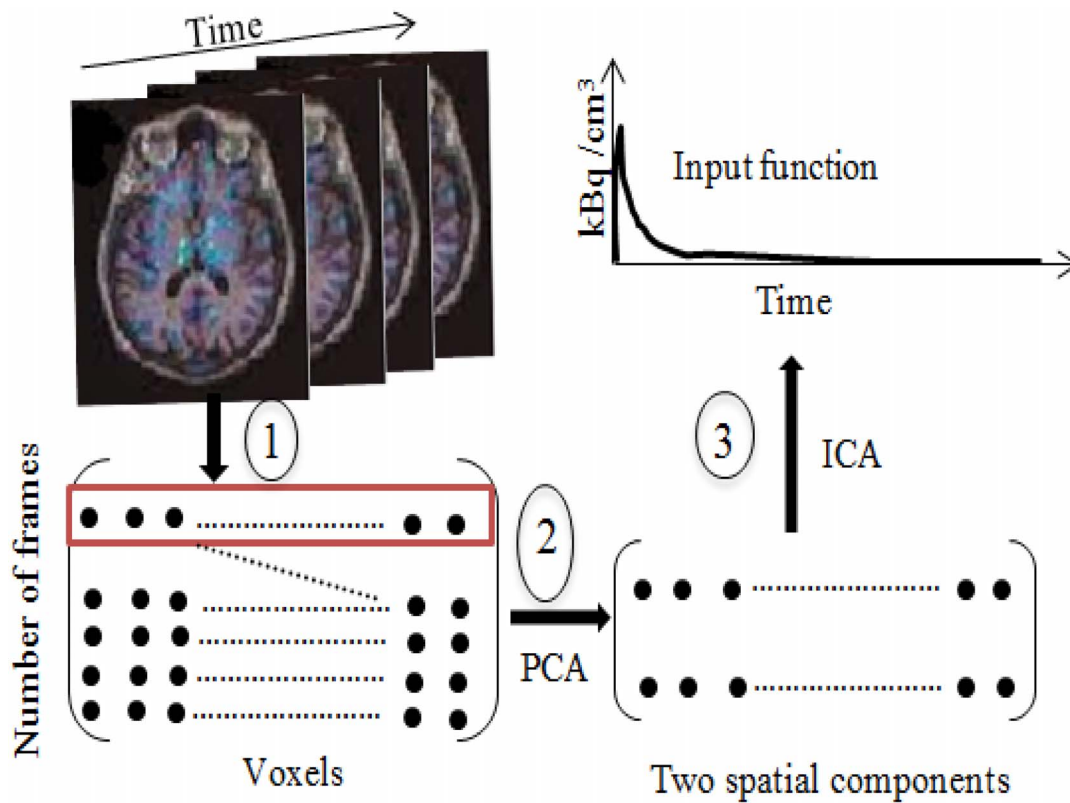
Fig. 3. Illustration of the ICA algorithm process steps. (1) the dynamic PET images derived from sequential measurement of the radioactivity are re-arranged into 2D matrix, the first dimension refers to time acquisition fames and the second dimension refers to the spatial distribution. (2) the principal component analysis reduce matrix dimension in order to keep the most significant activity (if columns of a mixture have relatively similar TACs, then, the corresponding columns tends to be estimated as one components). (3) update the de-mixing matrix until found convergence in separation between the two components.

$$l(\boldsymbol{W}) = -log|det(\boldsymbol{W})| - \sum_{j=1}^{Npx} \log P(\tilde{\boldsymbol{S}};\theta), \tag{4}$$

where $P(\tilde{\boldsymbol{S}};\theta)$ represents the distribution of the sources. Further detail on the calculation of $\boldsymbol{W}$ and the ADL parameters estimation are given in Appendix A and B in S1 File. A Summarize of ICA algorithm is given in appendix C in File S1.

8 Whole-blood calibration and input function generation

The whole-blood curves extracted from the ROIs by CS and ICA were calibrated to the ABSS-IF. Both curves were calibrated with one manual arterial blood sample taken at 15 minutes post-injection. In addition, a single inversion point at 1.5 minutes post-injection generated by the algorithm was corrected using one blood sample. The IFs were calculated using the derived whole-blood curves and the Hill function and bi-exponential function. The parameters of the two functions were calculated using an in-house software (Pharmacokinetic

Estimation for Radioligand Images (P.E.L.I)) which gives the possibility to model manual samples with different pre-defined function such as linear interpolation, mono-exponential, bi-exponential and Hill functions. Unlike ABSS-IF, the IDIFs were free from delay and dispersion effects.

9 Kinetic modelling

The total V_T which represents the ratio at the equilibrium of the concentration of radioligand in tissue to that in plasma (*i.e.* including the specific binding, nonspecific binding and free radioligand in tissue) was assessed. For the 2-TCM, V_T was defined as $DV = K_1/k_2(1+k_3/k_4)$ where $k_i(i=1\dots4)$ were the independent variables estimated by the compartmental model, as described elsewhere [41]. The weighted nonlinear fitting was performed with the Levenberg-Marquardt algorithm using an implemented trust-region. The cerebral blood volume was assumed in the trust-region function as 5% of the gray matter tissue [42]. The fitting curve and the brain data for each frame were weighted to the other frames using the trues Tr_i in the FOV, where i is the frame index as described by:

$$w_i = \frac{\left(t_i^e - t_i^s\right)^2}{dc^2 Tr_i}. \tag{5}$$

where t_i^s and t_i^e are the start and end time of the frame, respectively, and dc is the decay correction coefficient given by: $dc = \lambda_c\left(t_i^e - t_i^s\right)/e^{-\lambda_c t_i^e} - e^{-\lambda_c t_i^s}$ with $\lambda_c = 6.3 \times 10^{-2}$ per minute, that is the decay of ^{18}F.

10 Statistical analysis

The IFs derived by CS and ICA were compared to the ABSS-IF using the AUC ratio. Pearson correlation coefficients were used to evaluate the strength of the relationship between CS-IF, ICA-IF and ABSS-IF. Bland-Altman plot were performed to test the interchangeability of the V_T calculated by different methods in the temporal and frontal cortex, cerebellum, striatum, and the thalamus. The regression coefficients were tested using a one-sample t-test with statistical significance set to a value of $p < 0.05$. Repeated-measures ANOVA (RMANOVA) was performed using V_T values calculated using the IF from each method and according to their genotype (i.e. HAB and MAB subjects).

Results

1. Input Functions

The ABSS-IFs, CS-IF and ICA-IF curves demonstrated a substantial similarity in terms of shape for each individual subject. The peak activity of the CS-IF was reached at the same time as the ABSS-IF curve, but was notably smaller in amplitude. In contrast, the peak of the ICA-IF curve was reached slightly later
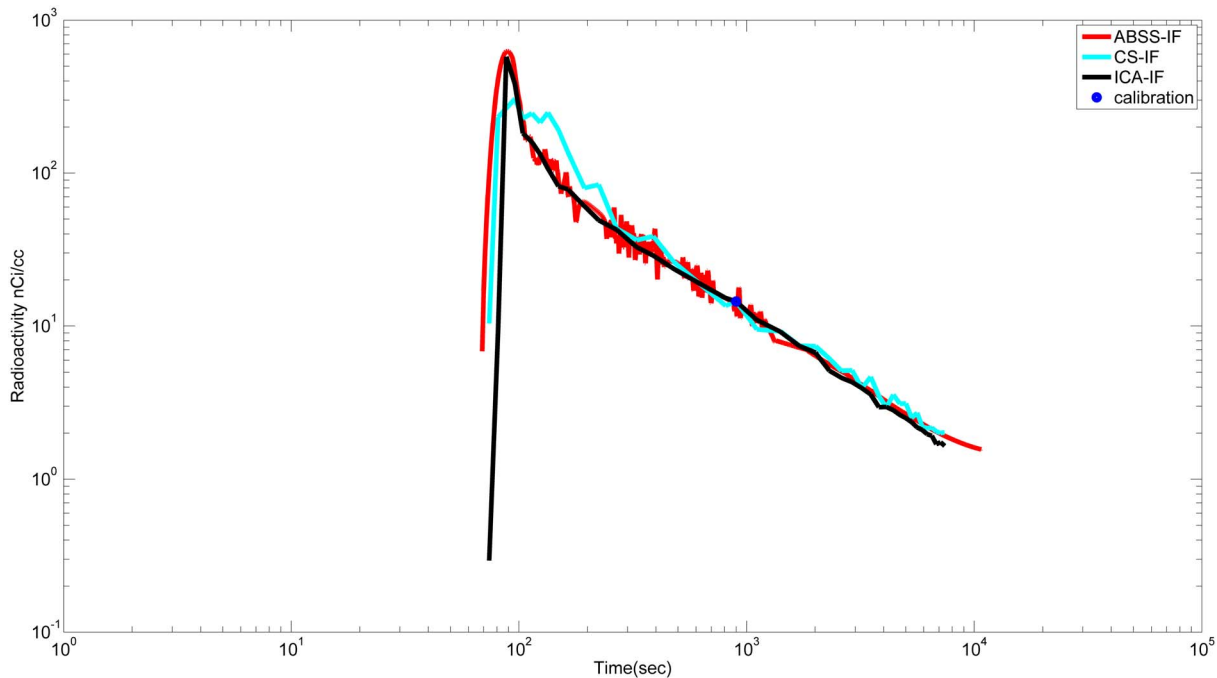
Fig. 4. A typical double logarithmic scale of the input function estimated by CS and ICA plotted against the ABSS-IF. Two arterial blood samples were used to correct for a small inversion at 1.5 minutes (green point) and to calibrate curves at 15 minutes post injection (blue point).

(~5 sec) and was much sharper than the ABSS-IF curve. Over the course of 15 minutes, the ABSS-IF and the two image-derived curves were similar (see Fig. 4).

Within each individual, the peak (blood activity in the first 180 seconds) and the tail (blood activity in the remaining time of scan) AUCs were calculated for the ABSS-IF, CS-IF and ICA-IF curves. The AUCs (mean $\pm$ SD) for the CS-IF peak were underestimated compared to the AUCs of the ABSS-IF peak (ratio=0.74$\pm$0.12). In contrast, the AUCs for ICA-IF peak were overestimated compared to the AUCs of the ABSS-IF peak (ratio=1.07$\pm$0.18). However, the ICA-IF and ABSS-IF tail AUCs ratio were very similar (ratio 1.03$\pm$0.10), whereas the CS-IF and ABSS-IF tail AUCs ratio were slightly overestimated (ratio=1.12$\pm$0.14).

2. Reliability of V_T Estimations

2.1 Group-wise comparisons between HAB vs. MAB

A group comparison for the frontal cortex is depicted in Fig. 5 (for the cerebellum, temporal cortex, striatum and thalamus see S1.1, S1.2, S1.3, and S1.4 Figs in S2 File). Within each group, the RMANOVA revealed no significant difference in V_T estimations from the ICA, CS and ABSS methods for HABs (F (2, 16)=0.2, p=0.82) and MABs (F (2, 16)=1.22, p=0.32), respectively.
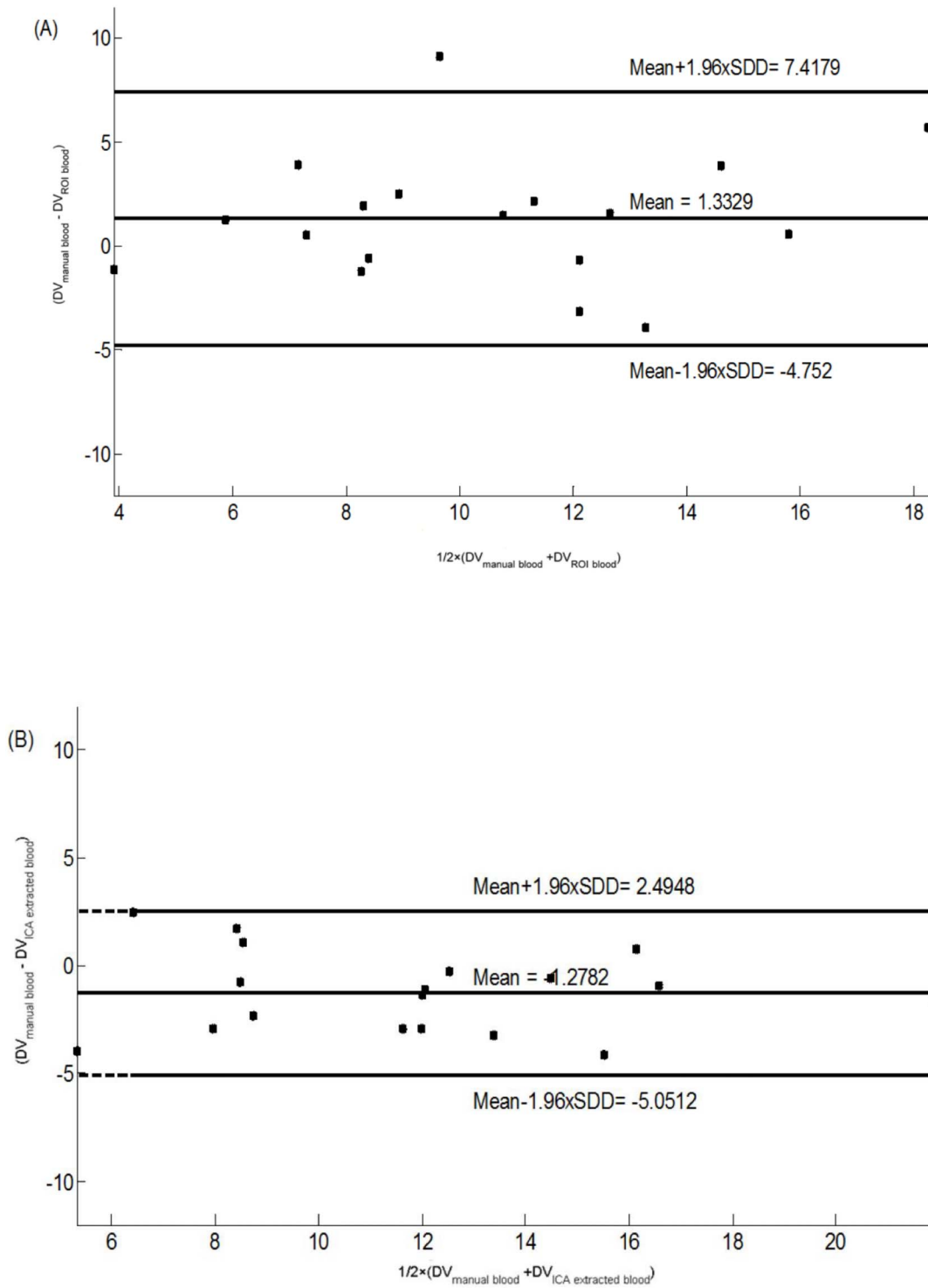
(A)

(B)

Fig. 5. Bland Altman plot of total distribution volume (V$_T$) in the frontal cortex comparing (A) ABSS-IF versus CS-IF, and (B) ABSS-IF versus ICA-IF. All candidates were within the 95% of limits agreed for V_T^{CS-IF} and V_T^{ICA-IF}, with the exception of one subject for V_T^{CS-IF}.

doi:10.1371/journal.pone.0115768.g005

Table 1. Results based on Regression Analysis V$_T$ calculated using CS-IF versus using ABSS-IF and V$_T$ calculated using ICA-IF versus using ABSS-IF.

	V$_T$ calculated using CS-IF *vs* V$_T$ using ABSS-IF					V$_T$ calculated using ICA-IF *vs* V$_T$ using ABSS-IF				
	r^2	b$_0$	b$_1$	*t*	*p*	r^2	b$_0$	b$_1$	*t*	*p*
Frontal cortex	0.71	1.13	0.85	4.01	0.0009	0.91	0.03	1.09	6.04	1.1E-04
Temporal cortex	0.70	0.34	0.95	5.19	8.8E-05	0.88	2.24	1.14	3.21	0.0053
Striatum	0.78	0.04	1.01	5.5	4.0E-05	0.89	1.64	1.05	3.74	0.0017
Thalamus	0.87	1.76	0.83	3.52	0.0027	0.92	-0.43	1.17	7.54	1.1E-06
Cerebellum	0.84	1.17	0.84	3.60	0.0023	0.90	0.98	1.01	4.37	0.0004

r^2: coefficient of determination, b$_0$: Intercept, b$_1$: Slope, *t*: t-test value, *p*: p-value.

doi:10.1371/journal.pone.0115768.t001

2.2 *Linear Regression*

We first conducted a simple linear regression analysis of the data (n=18) for frontal and temporal cortex, cerebellum, striatum and thalamus regions. Results of regression analysis comparing V$_T$s calculated using ICA-IF and V$_T$ calculated using ABSS-IF are shown in Table 1. Overall, V$_T$ using ICA-IF provided a more reliable estimation of gold standard V$_T$ using ABSS-IF (r^2>=0.88) than V$_T$ using CS-IF (r^2<0.88).

2.3 Bland Altman plot

The bias of the measurements between V$_T$ using ABSS-IF ($V_T^{ABSS-IF}$) and V$_T$ using CS-IF (V_T^{CS-IF}) calculated in the frontal cortex was 1.33 mL/cm^3 and the width of 95% of limits agreement was 12.17 mL/cm^3 containing 17/18 of difference scores (Fig. 6A) (for the cerebellum, temporal cortex, striatum, and thalamus see S2.1A, S2.2A, S2.3A, and S2.4A Figs, respectively, in S2 File). In contrast, the bias of the measurements between $V_T^{ABSS-IF}$ and V$_T$ using ICA-IF (V_T^{ICA-IF}) in the same region was −1.27 mL/cm^3 and the width of 95% of limits agreement was 7.54 mL/cm^3 containing all difference scores (18/18) (Fig. 6B) (for the cerebellum, the temporal cortex, the striatum, and the thalamus (see S2.1B, S2.2B, S2.3B, and S2.4B Figs, respectively, in File S2). Therefore, the magnitude of bias was smaller in V_T^{ICA-IF} than (V_T^{CS-IF}).

Discussion

In this study, we developed a new algorithm for the ICA method to extract the IF necessary for TSPO quantification in addition to the CS method used in other studies [22]. The extracted TACs from PET data include signals from both the parent and the metabolized radiotracers. Therefore, the blood TACs extracted from PET data need to be corrected to the blood-to-plasma ratio and, parent fraction of the radiotracer, which can be achieved by calibrating with one arterial or venous sample [18, 22, 43]. In this work, the whole-blood-to-plasma ratio was determined by fitting manual sample by a bi-exponential function, and the un-metabolized [^{18}F]-FEPPA activity was modeled by a Hill function because of the fast metabolism of this tracer as previously demonstrated [9, 16].
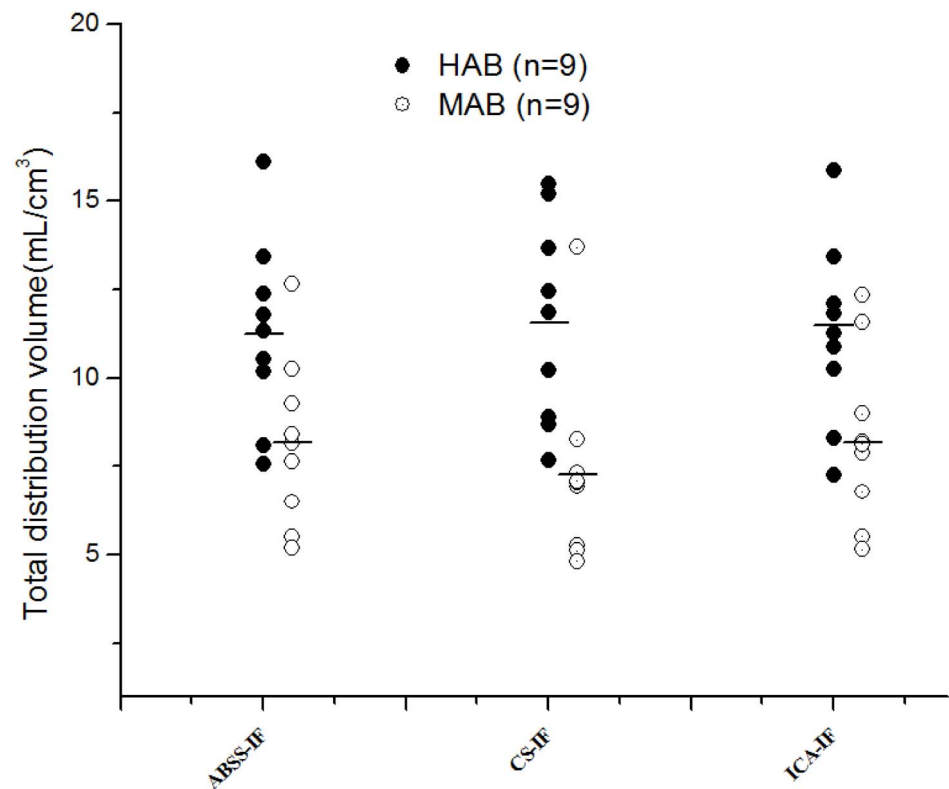
Fig. 6. Group comparison of total distribution volume (V$_T$) in the frontal cortex for high affinity binders (HABs) and mixed affinity binders (MABs) calculated respectively with ABSS-IF, CS-IF and ICA-IF.

The CS method was based on the segmentation of the carotid to extract blood activity. However, the identification of the internal carotid arteries requires high-resolution dynamic PET images or a co-registration with the subject MRI [23]. Due to the small size of the carotid and its elasticity (*i.e.* the artery can be stretched or bent during the MRI or PET scans), co-registration leads to an alignment error which requires further correction using a simple rigid body co-registration [23]. Therefore, the segmentation of the carotid in this study was carried out directly on OSEM+PSF [18F]-FEPPA PET which has been demonstrated to be robust against the partial volume effect [44]. The left and the right internal carotid were easily recognized in the early summed frames of a dynamic PET scan. Then, only a number of highest pixels (ten highest pixels) per plan were selected within the carotid ROIs to minimize the spill-in and spill-out effects. The number of pixels was established by experiment as performed elsewhere [22] and according to the spatial resolution of the scanner (in [22], Mourik et al used four highest pixels for [11C]-flumazenil PET data acquired using an ECAT EXACT HR+ scanner with spatial resolution=4.3mm at the center of FOV). The CS-IFs obtained are marginally compared to the ABSS-IFs and the AUCs ratio between CS-IF and the gold standard IF is low for the peak and high for the tail. In addition the inter-subject variation is high for both peak and tail

(0.12 and 0.14 respectively) although the scaling of the IF by a manual arterial sample to compensate the underestimation as suggested by Zanotti-Fregonara et al [23]. Despite the fact that the use of the highest pixels is simple, largely automatic and fully reproducible; this method is very sensitive to the motion effect and depends of the number of the selected high intensity volumes. Given that pixels ROI was defined on the average image over the two first minutes of scan, participant may move from its first location and, thus, leads to an inaccuracy in the blood TAC. Moreover, the tail of the IF plays an important role in VT variation when scans are long (120 to 180 minutes) and the metabolism is fast as in the case of FEPPA PET. As a result, the agreement between estimated V_Ts using CS-IF and ABSS-IF was only marginally significant ($0.70 \leq r2 \leq 0.87$) and the Bland Altman plot showed qualitative difference between $V_T^{ABSS-IF}$ and V_T^{CS-IF} which appear as a wide width of agreement limits (12.17 mL/cm^3). The source of this discrepancy includes potential contributors such as patient movement during the scans and the remaining partial volume effect, although it has been reduced by OSEM+PSF reconstruction algorithm.

The ICA method was used to derive the IF directly through a source signal de-mixing process. Unlike deterministic blind source separation (BSS) such as the non-negative matrix factorization (NMF), the ICA is more flexible and, therefore, able to model initial sources by different probabilistic distributions that accurately adapt to physical and physiological characteristics. The ICA algorithm was applied on *a priori* determined automatic anatomical segmentation of the brain vessel system. The advantage of collecting the activity from regions where the radiotracer activity in the blood is highly recognizable is to increase the number of samples and satisfy the Central Limit Theorem [43]. The segmentation was performed on PET data reconstructed with OSEM algorithm where the number of subsets=6 and the number of iterations=12, allowing for clear recognition of the high signal contrast of cerebral vessel activity to background noise. In doing so, however, there was some loss in precision of the tissue time activity. Especially, the application of ICA on the carotid region ROIs, fails to extract the IF. This is mainly due to the fact that the statistical property of mixture in segmented ROIs is violated (at least two distinct independent distributions built the mixture). Indeed, the segmented carotid ROIs is a mixture of arterial activity distribution and a random background noise distribution which led to the extraction of noisy curves (see.S3 Fig. in S2 File). In contrast, the activity within the whole-brain ROIs was assumed to be mixture of radiotracer activity in venous and the artery. The spatial distributions of these sources were slightly different because of several reasons. 1) the field of view of the scanner covers more voxels in venous than artery vessels; 2) the size of the venous cerebral vessels is large compared to the arterial ones which cause less partial volume error; 3) and likely due to the tracer binding to the vessel walls (i.e. the endothelium and smooth wall muscles).

Previously, researchers have used several different measures to calculate the independence from the mixed signal (*i.e.* kurtosis, entropy, mutual information, and the likelihood) [43]. In this study, we modeled the spatial distribution of blood activity through the PET acquisition time by an ALD. The choice of this

distribution is supported by the fact that the tracer is uniformly distributed in the venous vessels and arterial ones. In terms of voxel intensity, the histogram of the spatial distribution of both components was close to a Laplace distribution, which can be skewed to the left or right. The ALD was flexible through its skew parameter to fit this distribution (*i.e.* The two components were extracted as a first and a second independent source relative to the first and second principal components correspond to the highest eigenvalue). The first source closely resembled the ABSS-IF according to the peaked time and was visually identified as the desired arterial blood activity. It was subsequently used to generate the IF.

In further support of the ALDICA algorithm for [18F]-FEPPA PET data, it was compared to a non-parametric ICA based on the fast fixed-point EPICA algorithm, explained in detail elsewhere [24] (source code is freely available at http://home.att.ne.jp/lemon/mikan/EPICA.html), and a parametric ICA based on two distributions; a) ICA based on a Gaussian cost function and; b) an ICA based on maximum likelihood estimate and the general Gaussian distribution (GGD) [39]. The EPICA algorithm successfully extracts TAC from FDG PET data [23]. In case of [18F]-FEPPA PET data, however, this algorithm failed to extract the IF for several reasons. In the case of FDG PET, the blood-tissue histogram differentiates blood and tissue signal components and EPICA successfully emphasizes each component independently. In [18F]-FEPPA, however, this no longer the case as the histogram consists of two close distributions; venous and arterial blood signal in selected ROIs. EPICA failed in the separation of the two distributions in the selected ROIs because of their similarity with the applied cost function. The EPICA method works well with FDG due to its equal distribution in brain tissues, resulting in very similar tissue TAC scales and can be estimated as one component. In contrast, [18F]-FEPPA is not as equally distributed across tissues and hence, is difficult to separate blood from different tissue TAC scales. In the standardization process, the EPICA algorithm increased undesired signal (e.g. tissue component and noise). Moreover, the parameters of the cost function are fixed in the equation by the user and not by estimation from the data. For FDG PET data, as shown by Naganawa et al (2005), changing these parameters within a specified range ($10 < \lambda < 100$; $0.1 < m < 0.5$) did not influence the result. However, the parameters λ and m applied to [18F]-FEPPA PET data revealed a dependency on the selected values for the parameters. Further, we compared the ALD to other parametric spatial distribution models which, in general, are more flexible with manipulation of the data distribution. However, the Gaussian distribution was unappropriated to extract independent components because of the assumption made on the mixture (the mixture of independent components is more Gaussian than the independent components [43]). The GGD, in contrast, is more adaptable through its third parameter (shape parameter (SP)) and covers many distributions (SP<2, super-Gaussian distribution; SP=2, Gaussian distribution; SP>2, sub-Gaussian). The asymmetric distribution of ALDICA function allows for a good fit to the data compared to EPICA and the parametric models, as highlighted in Fig. 7. In summary, these comparisons support ALDICA as the spatial distribution function of choice in dynamic [18F]-FEPPA imaging.
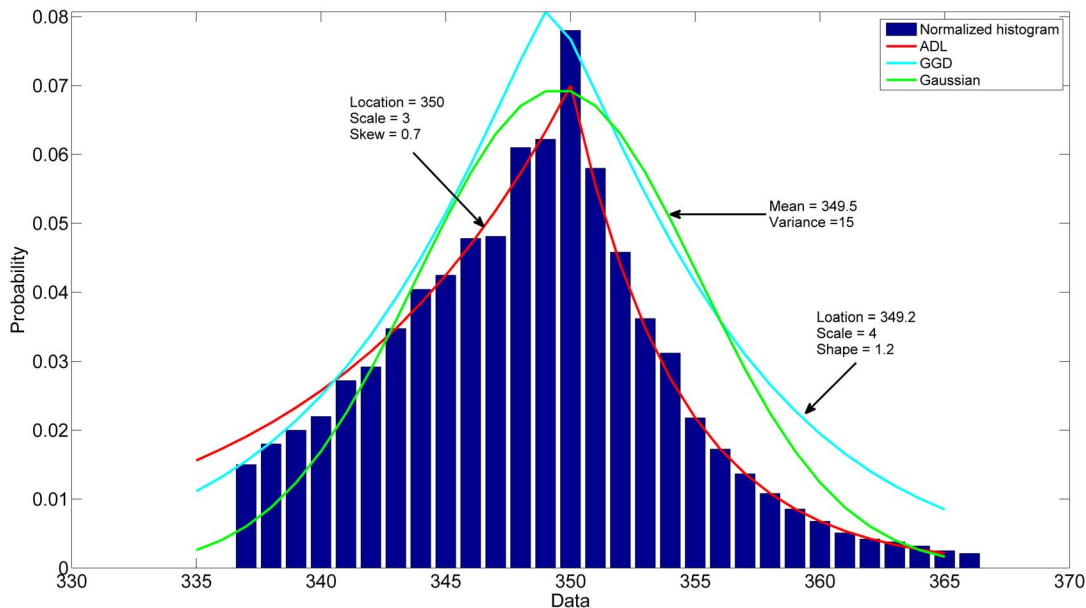
Fig. 7. Illustration of the normalized histogram of the first source, ADL, GGD, and Gaussian distributions respectively. The plot describes the data fit by three different distributions. The Gaussian distribution does not show a good model to represent data. The GGD fit better the sharper features of the histogram. However, it fails to fit well the asymmetry of data. The ADL is more appropriate to model the sharper feature of the histogram and, moreover, follows the asymmetric distribution of data through its skew parameter.

The obtained IFs, using ADLICA were similar to the ABSS-IF in shape, but not in magnitude. This was due to two ambiguities in the ICA algorithm: magnitude and permutation. To solve the magnitude issue, one manual blood sample was used to scale the extracted IFs at 15 minutes post-injection to calibrate the peak and the tail. The post-injection sample at 15 minutes was chosen due to the fact that, for [^{18}F]-FEPPA, this represents the near end of the tracer delivery to the tissue and the beginning of the blood clearance. Hence, at this time, the used plasma sample might be more accurate for calibration. The identification of the first and the second extracted components as arterial blood activity and venous or tissue activity was a sensitive task due to the permutation ambiguity of ICA. For the majority of the subjects (14/18), the magnitude of the second component, inspected visually, was higher than the first and peaked approximately 5 seconds later than the first component, which represent venous activity for reasons cited above (see.S4 Fig. in S2 File). For the remaining subjects (4/18), the second component appeared as a tissue activity shape which is explained by strong signal contamination of the blood region by surrounding tissue activity. In addition, for 2 of 18 subjects, the arterial blood activity was identified as the second component. Finally, a small single inversion point in the curve was created by the algorithm at ~1.5 minutes following tracer injection. Importantly, this inversion did not affect the estimated total VT values using IF. After correcting for calibration concerns, the peak AUCs and the tail AUCs calculated with ICA represent an promising estimation compared to those obtained with ABSS (peak

ratio$=1.07\pm0.18$, tail ratio$=1.03\pm0.10$). These estimations fall within an acceptable range of variation. Notably, the inter-subject variation is largely due to the threshold used to create the ROIs. We chose to keep this threshold constant (48% of maximum intensity) across all subjects. However, it is possible to reduce the variance by selecting a subject-specific threshold. In addition, the inter-frame motion is a hidden issue which is difficult to correct and contribute to the high variation of the tail ratios. In order to determine if the slight difference in peak activity timing between ICA-IF and ABSS-IF curves, we shifted the ICA-IF curve to the left to match the peaks. There was a negligible influence on the estimated V^{T} ($\sim$1% difference between V^{T} estimated with ICA-IF and the shifted ICA-IF). Moreover, V_{T} estimations obtained with ICA-IF were highly correlated ($0.88\leq r^{2}\leq0.92$) with ABSS-IF. The RMANOVA revealed no significant difference between $V_{T}^{ABSS-IF}$ and V_{T}^{CA-IF} Further, the Bland-Altman plot revealed only a negligible difference between $V_{T}^{ABSS\text{-}IF}$ and $V_{T}^{CS\text{-}IF}$ which appear as a small width of agreement limits (7.54 mL/cm^{3}).

Although the possibility of avoiding the use of ABSS to extract IF from PET data, arterial samples are usually needed to calculate the blood-to-plasma ratio and the un-metabolized radioligand. This issue should be addressed in further studies either by venous substitute [44] or by population base correction. Two other issues worthy to be addressed in this work. First the visual identification of the arterial blood activity and second the manual correction of the small inversion. Finally, a new methodology using clustering to extract a grey matter tissue reference region should be subject to future studies to quantify microglia activation using [^{18}F]-FEPPA as applied to [11C]-(R)-PK11195 tracer [45].

Conclusion

This study supports ICA from OSEM [^{18}F]-FEPPA PET as an interchangeable method to the gold standard ABSS to quantify TSPO in the human brain. The CS method produces slightly less accurate V_{T} and may, therefore, not be a reliable candidate as an alternative method to ABSS. The major advantage of these techniques is the extraction of IFs with low blood sampling and rapid processing time. Both ICA and CS methods were performed solely on PET image data, eliminating the need for MRI-based segmentation of blood regions. However, manual blood sampling was still required to calculate the metabolite and blood-to-plasma ratio, in addition to calibration. This limitation needs to be improved with future work.

Supporting Information

S1 File. Appendix A, B and C.
doi:10.1371/journal.pone.0115768.s001 (DOCX)

S2 File. This file contains the supporting information figures. S1.1 Fig: Direct comparison of total distribution volume (V_T) in the cerebellum for high affinity binders (HABs) and mixed affinity binders (MABs) calculated respectively with ABSS-IF, CS-IF and ICA-IF. S1.2 Fig: Direct comparison of total distribution volume (V_T) in the temporal cortex for high affinity binders (HABs) and mixed affinity binders (MABs) calculated respectively with ABSS-IF, CS-IF and ICA-IF. S1.3 Fig: Direct comparison of total distribution volume (V_T) in the striatum for high affinity binders (HABs) and mixed affinity binders (MABs) calculated respectively with ABSS-IF, CS-IF and ICA-IF. S1.4 Fig: Direct comparison of total distribution volume (V_T) in the thalamus for high affinity binders (HABs) and mixed affinity binders (MABs) calculated respectively with ABSS-IF, CS-IF and ICA-IF. S2.1 Fig: Bland-Altman plot of total distribution volume (V_T) in cerebellum region. S2.2 Fig: Bland-Altman plot of total distribution volume (V_T) in temporal cortex region. S2.3 Fig: Bland-Altman plot of total distribution volume (V_T) in striatum region. S2.4 Fig: Bland-Altman plot of total distribution volume (V_T) in thalamus region. S3 Fig: Log-Log scale plot of ABSS-IF and ICA-IF performed on carotid region. S4 Fig: Log-Log scale plot of the first and the second independent components.
doi:10.1371/journal.pone.0115768.s002 (DOC)

Author Contributions

Conceived and designed the experiments: AS R. Mizrahi SH. Performed the experiments: PR YK. Analyzed the data: R. Mabrouk. Contributed reagents/materials/analysis tools: R. Mabrouk PR. Contributed to the writing of the manuscript: R. Mabrouk MJ JK.

References

1. **Kreisl WC, Lyoo CH, McGwier M, Snow J, Jenko JK, et al.** (2013) In vivo radioligand binding to translocator protein correlates with severity of Alzheimer's disease. Brain 136: 2228–2238.

2. **Kreisl WC, Mbeo G, Fujita M, Zoghbi SS, Pike VW, et al.** (2009) Stroke incidentally identified using improved positron emission tomography for microglial activation. Arch Neurol 66: 1288–1289.

3. **Ouchi Y, Yoshikawa E, Sekine Y, Futatsubashi M, Kanno T, et al.** (2005) Microglial Activation and Dopamine Terminal Loss in Early Parkinson's Disease. Ann Neurol 57: 168–175.

4. **Gerhard A, Pavese N, Hotton G, Turkheimer F, Es M, et al.** (2006) In vivo imaging of microglial activation with [11C](R)-PK11195 PET in idiopathic Parkinson's disease. Neurobiology of Disease; 21: 404–412.

5. **Hirvonen J, Kreisl WC, Fujita M, Dustin I, Khan O, et al.** (2012) Increased In Vivo Expression of an Inflammatory Marker in Temporal Lobe Epilepsy. J Nucl Med 53: 234–240.

6. **Kreutzberg GW** (1996) Microglia: a sensor for pathological events in the CNS. Trends Neurosci 19: 312–318.

7. **Turner MR, Cagnin A, Turkheimer FE, Miller CCJ, Shaw CE, et al.** (2004) Evidence of widespread cerebral microglial activation in amyotrophic lateral sclerosis: an [^{11}C](R)-PK11195 positron emission tomography study. Neurobiology of Disease 15: 601–609.

8. Kreisl WC, Fujita M, Fujimura Y, Kimura N, Jenko KJ, et al. (2010) Comparison of [11C]-(R)-PK 11195 and [11C]PBR28, two radioligands for translocator protein (18 kDa) in human and monkey: Implications for positron emission tomographic imaging of this inflammation biomarker. NeuroImage 49: 2924–2932.

9. Wilson AA, Garcia A, Parkes J, McCormick P, Stephenson KA, et al. (2008) Radiosynthesis and initial evaluation of [^{18}F]-FEPPA for PET imaging of peripheral benzodiazepine receptors. Nucl Med Biol 35: 305–14.

10. Briard E, Zoghbi SS, Imaizumi M, Gourley JP, Shetty HU, et al. (2008) Synthesis and evaluation in monkey of two sensitive ^{11}C-labeled aryloxyanilide ligands for imaging brain peripheral benzodiazepine receptors in vivo. J. Med. Chem 51: 17–30.

11. Fujimura Y, Zoghbi SS, Simèon FG, Taku A, Pike VW, et al. (2009) Quantification of Translocator Protein (18 kDa) in the Human Brain with PET and a Novel Radioligand, ^{18}F-PBR06. J Nucl Med 50: 1047–1053.

12. Dollé F, Hinnen F, Damont A, Kuhnast B, Fookes C, et al. (2008) Radiosynthesis of [^{18}F]PBR111, a selective radioligand for imaging the translocator protein (18 kDa) with PET. J. Label Compd. Radiopharm 51: 435–439.

13. Maeda J, Suhara T, Zhang MR, Okauchi T, Yasuno F, et al. (2004) Novel Peripheral Benzodiazepine Receptor Ligand [11C]DAA1106 for PET: An Imaging Tool for Glial Cells in the Brain. Synapse 52: 283–291.

14. Boutin H, Chauveau F, Thominiaux C, Grégoire MC, James ML, et al. (2007) 11C–DPA-713: A Novel Peripheral Benzodiazepine Receptor PET Ligand for In Vivo Imaging of Neuroinflammation. J Nucl Med 48: 573–581.

15. Zhang MR, Kumata K, Maeda J, Yanamoto K, Hatori A, et al. (2007) 11C–AC-5216: A Novel PET Ligand for Peripheral Benzodiazepine Receptors in the Primate Brain. J Nucl Med 48: 1853–1861.

16. Rusjan P, Wilson AA, Bloomfield PM, Vitcu I, Meyer JH, et al. (2011) Quantitation of translocator protein binding in human brain with the novel radioligand [^{18}F]-FEPPA and positron emission tomography. J Cereb Blood Flow Metab 31: 1807–1816.

17. Jons HP, Ernst M, Hankerson J, Hardy K, Zamertkin JA (1997) Follow-up of Radial Arterial Catheterization for Positron Emission Tomography Studies. Human brain mapping 5: 119–123.

18. Mabrouk R, Dubeau F, Bentourkia M, Bentabet L (2012) Extraction of time activity curves from gated FDG-PET images for small animals' heart studies. Comput Med Imaging Graph 36: 484–491.

19. van der Weerdt AP, Klein LJ, Boellaard R, Visser CA, Visser FC, et al. (2001) Image-derived input functions for determination of MRGlu in cardiac F-18-FDG PET scans. J Nucl Med 42: 1622–1629.

20. Croteau E, Lavallee E, Labbe SM, Hubert L, Pifferi F, et al. (2010) Image-derived input function in dynamic human PET/CT: methodology and validation with (11)C-acetate and (18)F-fluorothioheptadecanoic acid in muscle and (18)F-fluorodeoxyglucose in brain. Eur J Nucl Med Mol Imaging 37: 1539–1550.

21. Backes H, Ullrich R, Neumaier B, Kracht L, Wienhard K, et al. (2009) Noninvasive quantification of (18)F-FLT human brain PET for the assessment of tumor proliferation in patients with high-grade glioma. Eur J Nucl Med Mol Imaging 36: 1960–1967.

22. Mourik EMJ, Lubberink M, Klumpers MHU, Comans EF, Lammertsma AA, et al. (2008) Partial volume corrected image derived input functions for dynamicPET brain studies: Methodology and validation for [11C]flumazenil Neuroimage 39: 1041–1050.

23. Zanotti-Fregonara P, Chen K, Liow JS, Fujita M, Innis RB (2011) Image-derived input function for brain PET studies: many challenges and few opportunities. J Cereb Blood Flow Metab 31: 1986–1998.

24. Naganawa M, Kimura Y, Ishii K, Oda K, Ishiwata K, et al. (2005) Extraction of a plasma time-activity curve from dynamic brain PET images based on independent component analysis. IEEE Trans Biomed Eng 52: 201–210.

25. Tomasi G, Edison P, Bertoldo A, Roncaroli F, Gerhard A, et al. (2008) Novel Reference Region Model Reveals Increased Microglial and Reduced Vascular Binding of ^{11}C-(R)-PK11195 in Patients with Alzheimer's Disease J Nuc Med 8 1249–1256.

26. Turheimer EF, Edison P, Paves N, Roncaroli F, Anderson NA, et al. (2007) Reference and target region modeling of [11C]-(R)-PK11195 brain studies. J Nucl Med 48: 158–167.

27. **Logan J, Fowler JS, Volkow ND, Wolf AP, Dewey SL, et al.** (1990) Graphical analysis of reversible radioligand binding from time-activity measurements applied to [N-11C-methyl]-(-)-cocaine PET studies in human subjects. J Cereb. Blood Flow Metab. 10, 740–747.

28. **Keming Y, Jin ZA** (2005) Three-Parameter Asymmetric Laplace Distribution and Its Extension. Communications in Statistics- Theory and Methods 34: 1867–1879.

29. **Owen DR, Gunn RN, Rabiner EA, Bennacef I, Fujita M, et al.** (2011) Mixed-affinity binding in humans with 18-kDa translocator protein ligands. J Nucl Med 52: 24–32.

30. **Mizrahi R, Rusjan PM, Kennedy J, Pollock B, Mulsant B, et al.** (2012) Translocator protein (18 kDa) polymorphism (rs6971) explains in-vivo brain binding affinity of the PET radioligand [(18)F]-FEPPA. J Cereb. Blood Flow Metab 32: 968–972.

31. **Lahiri DK, Nurnberger JI** (1991) A rapid non-enzymatic method for the preparation of HMW DNA from blood for RFLP studies. Nucleic Acids Res 19, 5444.

32. **Owen DR, Yeo AJ, Gunn RN, Song K, Wadsworth G, et al.** (2012). An 18-kDa translocator protein (TSPO) polymorphism explains differences in binding affinity of the PET radioligand PBR28. J Cereb. Blood Flow Metab. 32, 1–5.

33. **Sossi V, de Jong HWAM, Barker WC, Peter B, Ziad B, et al.** (2005) The second generation HRRT: a multi-centre scanner performance investigation. IEEE Nuclear Science Symposium Conference Record, 4: 2195–2199.

34. **Hong IK, Chung ST, Kim HK, Kim YB, Son YD** (2007) Ultra fast symmetry and SIMD-based projection-backprojection (SSP) algorithm for 3-D PET image reconstruction. IEEE Trans Med Imaging 26: 789–803.

35. **Comtat C, Bataille F, Michel C, Jones JP, Sibomana M, et al.** (2004) OSEM-3D reconstruction strategies for the ECAT HRRT. Nuclear Science Symposium Conference Record, IEEE.

36. **Rusjan P, Mamo D, Ginovart N, Hussey D, Vitcu I, et al.** (2006) An automated method for the extraction of regional data from PET images. Psychiatry Res 147: 79–89.

37. **Hilton J, Yokoi F, Dannals RF, Ravert HT, Szabo Z, et al.** (2000) Column-switching HPLC for the analysis of plasma in PET imaging studies. Nucl Med Biol 27: 627–30.

38. **Meyer E** (1989) Simultaneous correction for tracer arrival delay and dispersion in CBF measurements by the H2O15 autoradiographic method and dynamic PET. J Nucl Med 30: 1069–78.

39. **Mabrouk R, Dubeau F, Bentabet L** (2013) Dynamic Cardiac PET Imaging: Extraction of Time-Activity Curves using ICA and a Generalized Gaussian Distribution Model. IEEE Trans on Biomedical Engineering 60: 63–71.

40. **Amiri SI** (1998) Natural gradient works efficiently in learning. Neural Comput 10: 251–276.

41. **Innis RB, Cunningham VJ, Delforge J, Fujita M, Gjedde A, et al.** (2007) Consensus nomenclature for in vivo imaging of reversibly binding radioligands, J Cereb Blood Flow Metab 27: 1533–1539.

42. **Phelps ME, Huang SC, Hoffman EJ, Kuhl DE** (1979) Validation of tomographic measurement of cerebral blood volume with C-11-labeled carboxyhemoglobin. J Nucl Med 20: 328–334.

43. **Hyvarinen A, Oja E** (2000) Independent component analysis: Algorithms and application. Neural Networks 13: 411–430.

44. **Huhn A, Nics L, Baldinger P, Ungersbock J, Dolliner P, et al.** (2012) Combining image-derived and venous input function enables quantification of serotonin-1A receptor with [*carbonyl-^{11}C*] WAY-100635 independent of arterial sampling. Neuroimage 62: 199–206.

45. **Hsu PH, Hung IC, Kuo YJ, Hsu CC, Huang YE** (2012) Apply point spread functions in PET/CT image reconstruction: impact on standardized uptake value. Annal of nucl Med and Molecular imaging 25: 126–131.